DOI 10.24425/aee.2024.149924

Design and optimization of a radial-axial hybrid excited machine with spoke-type permanent magnet rotor

HONGBO QIU✉, WENHAO GAO, SHUAISHUAI DUAN

Zhengzhou University of Light Industry
China
e-mail: ✉ *332101050077@email.zzuli.edu.cn*

(Received: 04.09.2023, revised: 17.04.2024)

Abstract: To further enhance the speed regulation range of the hybrid excited machine (HEM), the structure of a magnetic ring is optimized using a combination of the magnetic circuit method (MCM) and numerical analysis method in this paper, and a disc magnetic ring (DMR) is proposed. The magnetic density distribution of the proposed disc magnetic ring hybrid excited machine (DMRHEM) is compared to the radial-axial hybrid excited machine (RAHEM), and the superiority of alleviating a saturation problem in the proposed DMRHEM is determined. To improve the power density, the spoke-type permanent magnet (PM) rotor is applied. The influence of the proposed DMR on the HEM is analyzed, and the field adjustment capability of the proposed DMRHEM is better. Based on this, by combining the bypass principle, the analytical expressions for the relations between the rotor pole-pair number and the motor axial length/stator inner diameter (MAL/SID) as well as flux regulation capability are derived to further explore the superiority of the proposed DMRHEM. The influence mechanism of the rotor pole-pair number and the MAL/SID on the proposed DRMHEM is determined. The optimal MAL/SID and pole-pair number are obtained.

Key words: disc magnetic ring, flux regulation capability, hybrid excitation, motor axial length/stator inner diameter, pole-slot combination

1. Introduction

Nowadays, permanent magnet (PM) machines have received extensive attention in academia and industry for lots of reasons [1]. However, its relatively fixed air-gap flux density and restricted flux regulation capability limit PM machines used in high-speed regions [2]. Hence, in recent years, the improvement of field adjustment capacity in the PM machines has been a hot spot.

For the shortage of flux regulation capability in the PM machine, the hybrid excited machine is proposed, which add the electric windings based on the PM machines and could adjust the air-gap magnetic field [3–5]. The flux regulation capability of the HEM has always been the focus and difficulty, which has attracted many scholars to study it [6, 7]. Moreover, the improvement of the HEM structure has always been an important part of further enhancing the flux regulation range [8, 9]. The current improvement of HEM structure focus on the whole structure or the distribution of PMs [10]. For example, Wang proposed an AC hybrid-excitation PM machine with an axial stator. Since the magnetic path in the radial stator and axial stator are parallel, the *d*-axis in the machine is large, which is beneficial to the flux-weakening capability. In addition, the flux regulation ratio gets smaller if the stack length of the radial stator gets larger [11]. In [12], an axial-radial stator PM machine is proposed. In this case, the excitation winding is located in the axial stator. In [13], the hybrid excited motor with an axial shunt rotor is proposed. Its flux density is large. However, due to the single end excitation, the flux regulation range is restricted. In [14], the axial magnetic shunt stator design is proposed, which could improve the power density, and the flux regulation range is increased by the double end excitations. However, the excitation coils and armature coils are placed on the stator, which results in the heat dissipation difficulty. In [15], the flux–torque regulation hybrid excitation machine is proposed. Its axial magnet magnetomotive force (MMF) is caused by the periodical alternating current. The magnetic field and principle are complex, thus the motor control is difficult. Moreover, since the effective area of the axial magnetic circuit is small, the flux regulation range is restricted.

The magnetic rings are the effective area of the axial magnetic circuit and the important structure to link the PM excitation and electric excitation. However, there is little research on the optimization of magnetic rings. In this paper, a radial-axial hybrid excited machine with a spoke-type PM rotor is presented. There are two excitation sources in RAHEMs, so the radial and axial magnetic paths are coupled, and the flux distribution is complex. Moreover, a precise 3-D model is adopted. The important structure of the axial flux path, i.e. the magnetic rings are optimized by the field-to circuit method to enhance the field adjustment range of the RAHEM, and the disc magnetic ring is proposed. First, the magnetic density distribution of the proposed DMRHEM is compared to the RAHEM, and the superiority of an alleviating saturation problem in the proposed DMRHEM is determined. Then, by studying the air-gap flux regulation capability with different machines, the influence mechanism of the proposed DMR on flux regulation capability is determined, and the proposed DMRHEM has better flux regulation performance. On this basis, in order to further explore the superiority of the proposed DMRHEM, by combining the bypass principle, the analytical expressions for the relations between the rotor pole-pair number and the motor axial length/stator inner diameter (MAL/SID) as well as flux regulation capability are derived. For these two key parameters, by investigating the proposed DMRHEM with a different rotor pole-pair number and MAL/SID, the influence mechanism of the rotor pole-pair number and the MAL/SID on flux regulation capability in the proposed DRMHEM is determined. Furthermore, the optimal MAL/SID and pole-pair number are obtained.

2. The finite element method

The whole machine is selected as the solved region, and a three-dimensional model is established by the finite element method. Then the model is meshed by taking a tetrahedron as an element shape. The models were established by the ANSYS2021R1 software with a guarantee

of mesh quality. Meanwhile, the mesh numbers are 200 000, and the time steps are 0.1 ms. The residual value is 0.005. Br and Hc of the PM is 1.2 T and –890 000 A/m. The mesh of the RAHEM is shown in Fig. 1.

The three-dimensional finite element method divides the magnetic field region into a finite number of tetrahedral elements. Nodes are formed from elements. The vector bits within a tetrahedral element are linear interpolation functions of its vertex vector bits.

The air gap magnetic density of the motor plays a major role in the simulation results, so the grid encryption process should be carried out at the air gap, and two layers of air domain are set up to make the division of the motor air gap more uniform and detailed. The boundary condition is the Neumann boundary. The direction of the magnetic field is tangential to the surface, and no magnetic flux passes through. The stacking factor of the laminated cores is 0.98, and the stacking direction is the Z-axis.

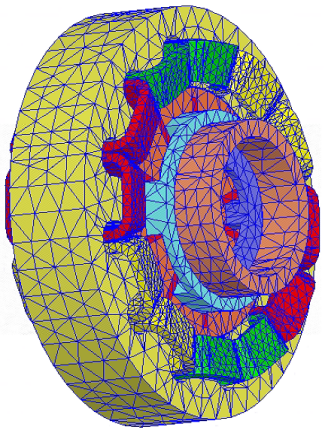

Fig. 1. The mesh of the RAHEM

3. Machine topologies and operating principle

There are: a spoke-type PM rotor, a fractional-slot stator, two N-pole and S-pole magnetic rings in the RAHEM, as given in Fig. 2. The magnetic rings are fixed onto the rotor and fabricated from Steel-1010, which has strong mechanical strength. The axial air-gap between the axial field excitation coils (FCs) and the magnetic ring is 0.5 mm. The armature windings are fed by an AC power supply, and the axial FCs fed by a DC power supply are fixed in the end caps, not increasing the axial length. Therefore, they could be separately controlled. The FCs will produce a pair of magnetic poles. The magnetic field generated by the magnetic pole is distributed to each pole area of the rotor through the magnetic ring claws, and the magnetic field of the N- and S- poles in the RAHEM could be adjusted.

Moreover, the heat from the windings could influence the reliability of the RAHEM. Compared to the axial magnetic stator shunt motor with excitation windings fixed on the stator [14], the influence is smaller. Besides, the heat from the FCs in the RAHEM could be cooled by the heat dissipating device linked with end caps. The material of the RAHEM is listed in Table 1.

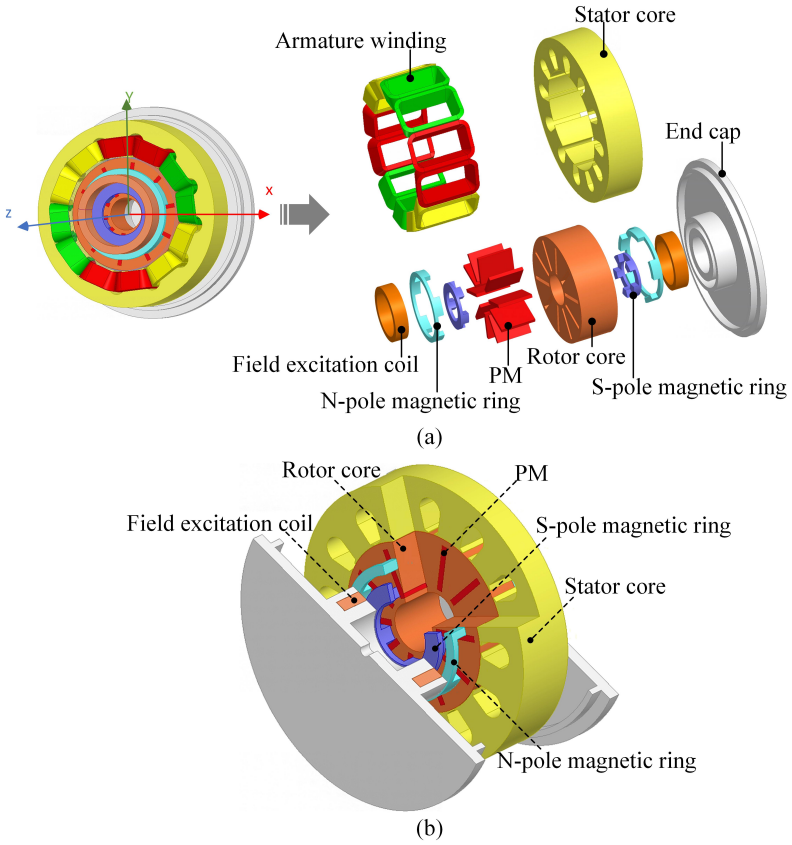

Fig. 2. Machine topology: (a) assembly drawing; (b) 3-D cut drawing

Table 1. Materials of the RAHEM

Item	**Material**
Stator	DW310
Rotor	Steel-1010
N-pole magnetic ring	Steel-1010
S-pole magnetic ring	Steel-1010
End cap	Steel-1010
Permanent magnets	N35
Field excitation windings	copper
Armature winding	copper

In the 12-slot/10-pole RAHEM, the 3-D magnetic paths are illustrated in Fig. 3. There are some excitation states, that is, "PM merely work", "Positive MMF work", and "Negative MMF work". To demonstrate clearly, the axial device at one end is ignored and a part of the structure is specified. The corresponding equivalent magnetic circuits (EMCs) are also demonstrated in Fig. 3, where R_{PM} is the reluctance of the PM, R_{ro} is the reluctance of the rotor core, R_{st} and R_{sy} are the reluctances of the stator tooth and stator yoke, R_{gr} and R_{ga} are the reluctances of the radial air gap and axial air gap, R_{Nr}, R_{Sr}, R_{ec} are the reluctances of the N-pole magnetic ring, S-pole magnetic ring and end cap, respectively. F_f and F_{PM} are the magnetomotive force (MMF) of the FCs and PMs.

According to Fig. 3(a), with the "PM merely work" excitation condition, the PM flux passes by air-gaps. It agrees with the conventional PMSM. It should be noted that the axial magnetic path is the PM N-pole → rotor core → S-pole magnetic ring→ magnetic end region → N-pole magnetic ring → PM S-pole. Therefore, the flux in the radial magnetic path of the conventional PMSM, which could result in the saturation problem, can flow along the axial magnetic path in the RAHEM. Then, as depicted in Fig. 3(a), the flux linkage Φ_{PM} with the "PM merely work" excitation can be obtained as:

$$\Phi_{\mathrm{PM}} = N_c \times \frac{F_{\mathrm{PM}} - \dfrac{F_{\mathrm{PM}} \times (R_{\mathrm{PM}} + R_o)}{\left(R_{\mathrm{PM}} + R_o + \dfrac{\left(\dfrac{R_r}{2} \times R_a\right)}{\left(\dfrac{R_r}{2} + R_a\right)}\right)}}{R_a}, \tag{1}$$

where R_r is the sum of $2R_{gr}$, $2R_{st}$, R_{sy} and R_{ro}, R_a is the sum of R_{Sr}, R_{Nr}, R_{ec}, $2R_{ga}$. N_c is the number of turns of the stator armature coil. From (1) we can see that Φ_{PM} could rely on R_r and be affected by R_a.

With the negative axial excitation (AE) current in the FCs, the direction of the AE flux is corresponding with the axial PM flux but it is different to the radial PM flux as depicted in Fig. 3(b). Furthermore, it could weaken the flux density of the air-gap. As for Fig. 3(b), the relative EMC is illustrated, the flux linkage Φ_{fw} with the "Negative MMF work" excitation can be demonstrated as:

$$\Phi_{fw} = \Phi_{\mathrm{PM}} - N_c \times \frac{2F_f}{R_r + R_a}. \tag{2}$$

The field weakening capability $\Delta\Phi_{fw}$ could be given as:

$$\Delta\Phi_{fw} = \Phi_{\mathrm{PM}} - \Phi_{fw} = N_c \times \frac{2F_f}{R_r + R_a}. \tag{3}$$

$\Delta\Phi_{fw}$ is reduced with the increment of the total of R_a and R_r. With the positive AE current, two Positive MMF works can be obtained, which rely on the axial MMF in the FCs. With the small axial MMF, as depicted in Fig. 3(c), since the AE flux direction is different from the axial PM flux, a portion of the axial flux is forced through the radial flux flowing path, d enhancing the armature magnetic field. It is referred to as "Positive MMF work-a", and its EMC is demonstrated in Fig. 3(c). The flux linkage Φ_{fe1} with the "Positive MMF work-a" excitation could be calculated

as:

$$\Phi_{fe1} = \Phi_{\mathrm{PM}} + N_c \times \frac{2F_f}{R_r + R_a}. \tag{4}$$

The field enhancing capability $\Delta\Phi_{fe1}$ can be expressed as

$$\Delta\Phi_{fe1} = \Phi_{fe1} - \Phi_{\mathrm{PM}} = N_c \times \frac{2F_f}{R_r + R_a}. \tag{5}$$

It can be found that the $\Delta\Phi_{fe1}$ is inversely related to the total of R_a and R_r. Nevertheless, the saturation problem in the axial magnetic path with the field enhancing is smaller than that under the field weakening. Therefore, the field enhancing capability is better than the field weakening capability.

With the large enough axial positive MMF, the AE flux through the air-gap will enhance the field as illustrated in Fig. 3(d). It could be referred to as "Positive MMF work-b". Consequently, as shown in Fig. 3(d), the flux linkage Φ_{fe2} under the "Positive MMF work-b" could be given as:

$$\Phi_{fe2} = N_c \times \left(\frac{F_{\mathrm{PM}}}{R_a + R_{\mathrm{PM}} + R_{ro}} + \frac{2F_f}{R_r + R_a} \right). \tag{6}$$

It can be seen that because Φ_{fe2} is larger than Φ_{fe1} and the first item of (6) is larger than Φ_{PM}, the field enhancing capability of work-b is better than that of work-a. Nevertheless, we should focus on the saturation problem of the magnetic ring under the "Positive MMF work-b" excitation.

For calculating Φ_{PM}, Φ_{fw}, and Φ_{fe1}, the reluctance and MMF in the magnetic circuits could be expressed as:

$$R = \frac{l}{\mu_{ri}\mu_0 S}, \tag{7}$$

$$F_{\mathrm{PM}} = \frac{B_r w_{\mathrm{PM}}}{\mu_{r\mathrm{PM}}\mu_0}, \tag{8}$$

$$F_f = \frac{N_f i_f}{6}, \tag{9}$$

where μ_{ri} is the core relative permeability, $\mu_{r\mathrm{PM}}$ is the PM relative permeability, μ_0 is the vacuum relative permeability. B_r and w_{PM} are the remanence and the magnetization thickness of the PM. N_f is the number of turns of the AE coil, and i_f is the AE current. Then, the phase no-load back-EMF E_m could be given as:

$$E_m = N_{paw} \times \frac{\Delta\Phi}{\Delta t}, \tag{10}$$

where N_{paw} is the armature coil number.

Therefore, the field adjustment capability could be expressed by the field adjustment ratio k_Φ, which is given as:

$$k_\Phi = \frac{E_{fe1}}{E_{fw}} \times 100\%, \tag{11}$$

where E_{fw} and E_{fe1} are the amplitude of the phase no-load back-EMF under the "Negative MMF work" and "Positive MMF work-a". By the EMC method, the back-EMF and the field adjustment capability of the RAHEM can be calculated, and compared to the finite element method (FEM) results. The calculated field adjustment capability by the MCM is consistent with the FEM results as depicted in Table 2.

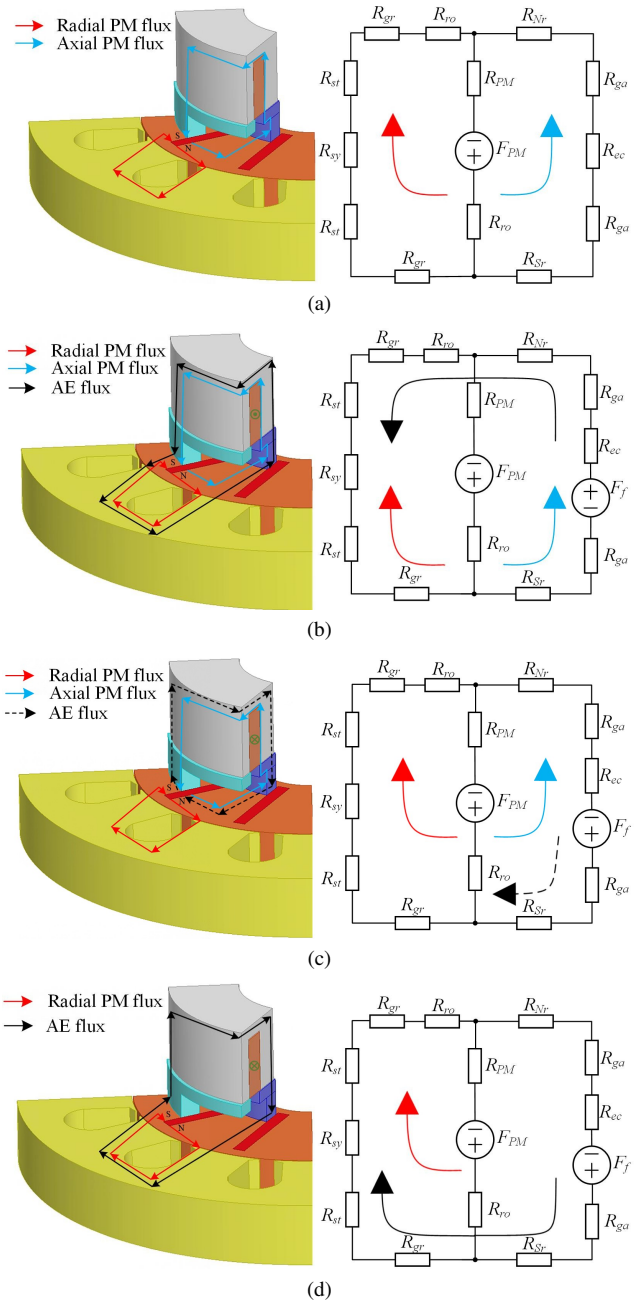

Fig. 3. Diagram of the flux flowing in the RAHEM: (a) PM merely work; (b) negative MMF work; (c) positive MMF work-a; (d) positive MMF work-b

Table 2. Calculation results by EMC and FEM method

Excitation condition	No-load back-EMF, E_m (V)		Flux regulation ratio, k_Φ	
	EMC	FEM	EMC	FEM
PM merely work	168.6	182	153%	156%
Negative MMF work	166.4	181.4		
Positive MMF work-a	215.8	236.7		

4. Proposed disc magnetic ring

4.1. Saturation problem

Based on (1), (3), (5), the axial magnetic reluctance not only confines the PM flux but also affects the field weakening and enhancing capability of the RAHEM. It should be noted that when the excitation coil generates axial magnet magnetomotive force (MMF), the axial flux enters the main air-gap through the axial air-gap, magnetic ring and the rotor core, which could adjust the radial magnetic field. Due to the narrow magnetic circuit of the axial device, the teeth of magnetic rings will be oversatured, when the AE current is increased. The flux density distribution of the rotor and magnetic ring in the RAHEM with –5 A AE current is shown in Fig. 4. It is concluded that the unbalanced distribution of the magnetic ring structure result in the rotor magnetic density unbalanced distribution. Due to the partial oversaturation of the magnetic ring, the flux regulation capability of the RAHEM is restricted.

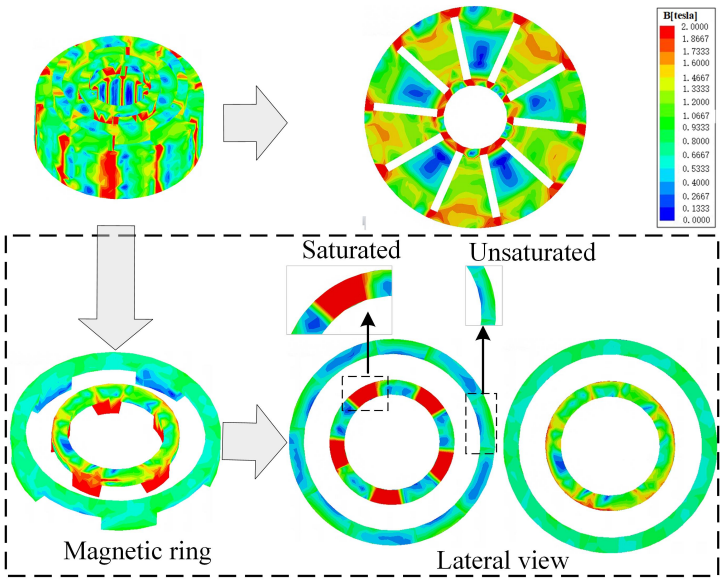

Fig. 4. Flux density distribution of rotor and magnetic ring of the RAHEM with –5 A AE current

Consequently, the optimization of magnetic rings is necessary. Therefore, this paper proposed a disc magnetic ring shown in Fig. 5, and its internal diagram is depicted in Fig. 6. The proposed magnetic ring is in the bottom of the rotor core. Its axial length is reduced from 15 mm (RAHEM)

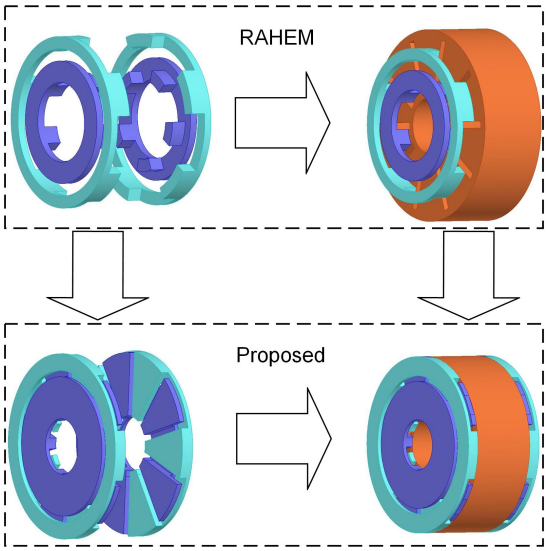

Fig. 5. Proposed disc magnetic ring structure

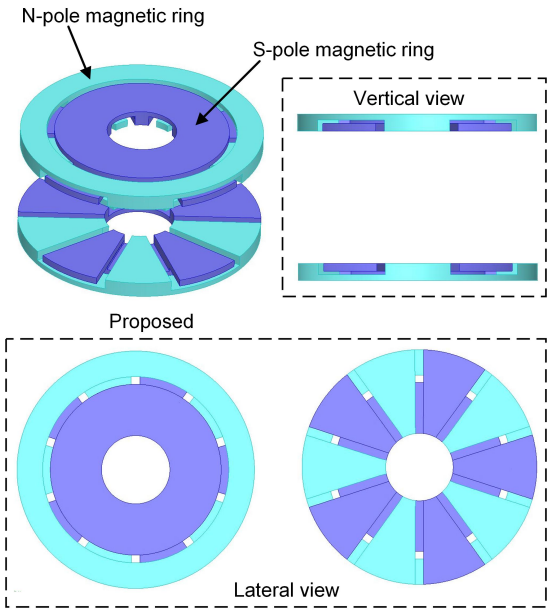

Fig. 6. Internal diagram of proposed disc magnetic ring structure

to 9 mm (DMRHEM), reduced by 40%. This flat design not only reduces the overall axial length of the motor, but also reduces the reluctance of the magnetic circuit in the axial device, which alleviates the oversaturation of the magnetic rings in Fig. 4, and thus the utilization ratio of the axial MMF is increased. The magnetic density distribution of the rotor and proposed DMR with –5 A AE current is shown in Fig. 7. The oversaturation of the partial magnetic ring in Fig. 4 is alleviated in the proposed DMRHEM. Therefore, the flux will be further weakened by a larger negative AE current from the excitation coil. As a result, the flux weakening capacity of the proposed DMRHEM is better, and its flux regulation scope, i.e., the speed regulation range of the machine is larger.

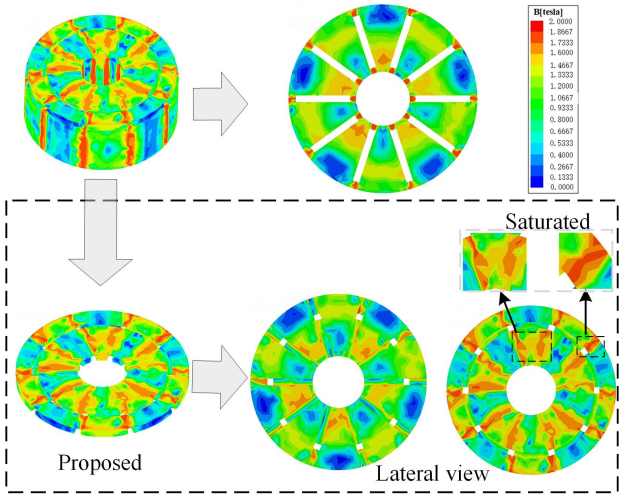

Fig. 7. Magnetic density distribution of rotor and proposed DMR with –5 A AE current

4.2. Performance comparison with different structure

To verifying the superiority of the proposed DMRHEM, the variation of air gap flux density with various magnetic rings versus excitation current based on the FEM is obtained.

According to Fig. 8, the flux weakening range of air gap flux density in the RAHEM is 0.01 T, the flux enhancing range is 0.17 T. The whole adjustment range is 0.18 T. Besides, the flux weakening range of air gap flux density in the proposed DMRHEM is 0.09 T, the flux enhancing range is 0.35 T. Its whole adjustment range is 0.44 T, which is 2.4 times than that of the RAHEM.

Hence, the field adjustment performance is enhanced in the proposed DMRHEM. Moreover, the proposed DMRHEM overcomes the shortage of flux weakening capability in the RAHEM. Its flux weakening range is 9 times than that of the RAHEM.

The back-EMFs with various magnetic rings are demonstrated in Fig. 9. As for the proposed DMRHEM, the maximum of back-EMF is 170 V, the minimum is 70 V, and the variation range is 100 V. In the RAHEM, the maximum of back-EMF is 162 V, the minimum is 120 V, and the variation range is 42 V. Therefore, the variation range of back-EMF in the proposed DMRHEM is larger than that of the RAHEM.

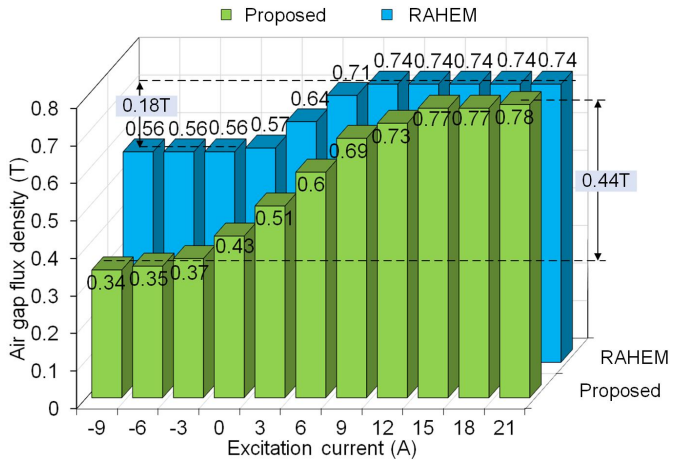

Fig. 8. Variation of air gap flux density with various magnetic rings versus excitation current

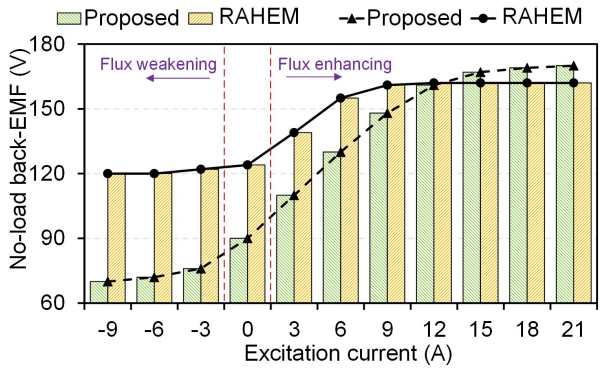

Fig. 9. Variation of no-load back-EMF with different magnetic rings versus excitation current

The structure parameters and numerical calculation results with different magnetic rings are illustrated in Table 3.

Table 3. Structure parameters and numerical calculation results

Parameter	Proposed DMRHEM	RAHEM	Unit
Axial length	9	15	mm
N-pole ring radius	65.5	56	mm
Contact area with rotor	10 620	2 000	mm^2
Volume	173 200	99 300	mm^3
Flux regulation ratio	230%	156%	

5. Influence of key parameters

To further improve the field adjustment range and the PM utilization rate in the proposed DMRHEM, some key parameters are designed in this portion.

A schematic diagram of a bypass effect structure principle is shown in Fig. 10.

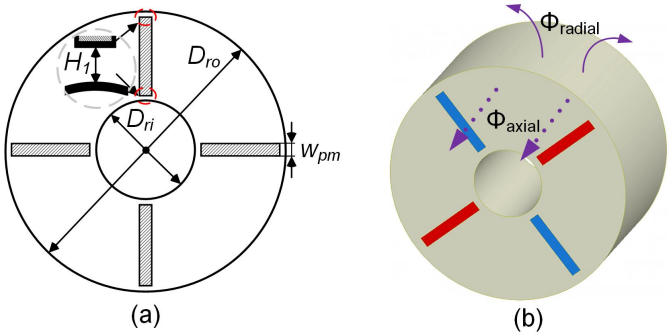

Fig. 10. Schematic diagram of bypass effect structure principle: (a) section view; (b) 3-D view

The air gap flux density of the rotor surface in radial magnetic circuit Φ_{radial} can be given as:

$$\Phi_{\text{radial}} = \pi D_{ro} \times l_{Fe} \times B_{\delta}\,, \tag{12}$$

where D_{ro} is the rotor outer diameter, B_{δ} is the air gap flux density, l_{Fe} is the rotor core length, and the air gap flux of the rotor cross section in the axial magnetic circuit Φ_{axial} can be demonstrated as:

$$\Phi_{\text{axial}} = \left[\frac{\pi(D_{ro}^2 - D_{ri}^2)}{4} - p \times (D_{ro} - D_{ri} - 2H_1) \times w_{\text{PM}}\right] \times B_{\text{axial}}\,, \tag{13}$$

and $\dfrac{\Phi_{\text{axial}}}{\Phi_{\text{radial}}}$ can be expressed as:

$$\frac{\Phi_{\text{axial}}}{\Phi_{\text{radial}}} = \frac{\left[\dfrac{\pi(D_{ro}^2 - D_{ri}^2)}{4} - p \times (D_{ro} - D_{ri} - 2H_1) \times w_{\text{PM}}\right] \times B_{\text{axial}}}{\pi D_{ro} \times l_{Fe} \times B_{\delta}}\,, \tag{14}$$

where D_{ri} is the rotor inner diameter, B_{axial} is the flux density of the rotor cross section in the axial magnetic circuit, p is the rotor pole-pair number, H_1 is the distance between the inner or outer diameter of the rotor and PM. When D_{ri} and H_1 are neglected, consider the influence of p and w_{pm}, $\dfrac{\Phi_{\text{axial}}}{\Phi_{\text{radial}}}$ can be expressed as:

$$\frac{\Phi_{\text{axial}}}{\Phi_{\text{radial}}} = \left(1 - \frac{1}{\dfrac{\pi D_{ro}}{2pw_{pm}} - 1}\right) \times \frac{1}{4} \times \frac{D_{ro}}{l_{Fe}} \times \frac{B_{\text{axial}}}{B_{\delta}}\,. \tag{15}$$

B_{axial} is restricted by the saturation characteristics of the rotor and it cannot be too high (for example, 10 steel is about 2 T). According to the motor design, B_δ has a reasonable value (about 1 T). Thus $\dfrac{B_{\text{axial}}}{B_\delta}$ keeps constant. The DMRHEM with larger axial flux, tend to contribute to the better bypass effect. Therefore, the magnetic field regulation range will be wider, and the air gap flux regulation ratio k_Φ will be larger. Accordingly to (15), the relationship can be expressed as:

$$\begin{cases} \dfrac{D_{ro}}{l_{Fe}} \uparrow \Rightarrow \dfrac{\Phi_{\text{axial}}}{\Phi_{\text{radial}}} \uparrow \Rightarrow k_\Phi \uparrow \\ p \uparrow \Rightarrow \dfrac{\Phi_{\text{axial}}}{\Phi_{\text{radial}}} \downarrow \Rightarrow k_\Phi \downarrow \end{cases} . \tag{16}$$

The MAL/SID can be defined as $k_\lambda = \dfrac{l_{Fe}}{D_{\text{sin}}}$. Based on the above theoretical derivation, it can be observed that the variation of the MAL/SID k_λ and the rotor pole-pair number p will affect $\dfrac{\Phi_{\text{axial}}}{\Phi_{\text{radial}}}$, and the air gap flux regulation ratio k_Φ, which is shown in Fig. 11.

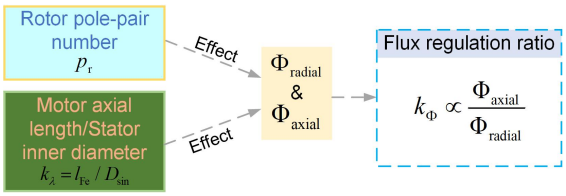

Fig. 11. Design relationship between the rotor pole-pair number, k_λ (motor axial length/ inner diameter) and k_Φ (flux regulation ratio)

5.1. Motor axial length/ inner diameter

On the basis of the above analysis, the influence of various k_λ on the field adjustment performance in the proposed DMRHEM is studied. The stator inner diameter D_{sin} and rotor core length l_{Fe} of the motor are the main structural parameters. $D_{\text{sin}}^2 l_{Fe}$ can reflect the effective volume, which could affect the output power. Then, when studying the influence of different k_λ on the flux regulation performance in the proposed DMRHEM, keeping $D_{\text{sin}}^2 l_{Fe}$ as a constant, the stator outer diameter changes accordingly. The structure parameters and numerical calculation results with different k_λ are illustrated in Table 4.

Table 4. Structure parameters and numerical calculation results with different k_λ

Parameter	k_λ **= 0.98**	k_λ **= 0.57**	k_λ **= 0.36**	k_λ **= 0.24**	k_λ **= 0.17**	**Unit**
Stator outer diameter	190	210	230	250	270	mm
Stator inner diameter	100	120	140	160	180	mm
Core length	100	68.4	50	38.28	30.25	mm
Flux regulation ratio	131%	150%	230%	250%	350%	

According to Fig. 12(a), the variation of air gap flux density with different k_λ versus excitation current is analyzed.

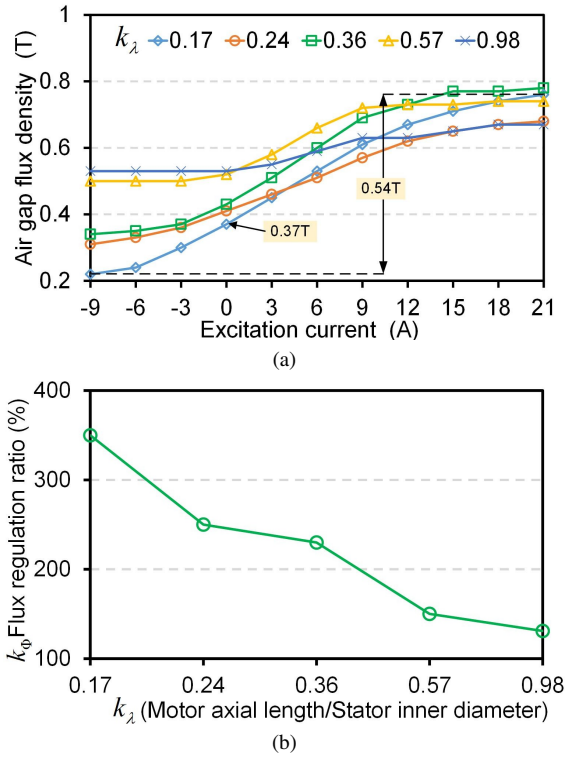

Fig. 12. Air gap flux regulation characteristic curves with different k_λ: (a) variation of air gap flux density with excitation current; (b) variation of flux regulation ratio k_Φ with k_λ

According to Fig. 12(a), the variation of air gap flux density with different k_λ versus excitation current is analyzed. With the "PM merely work", the air gap flux density of k_λ (0.98) is the largest, and the k_λ (0.17) one is the lowest. With the negative 9 A excitation current, the k_λ (0.17) one is also the lowest. With the positive 21 A excitation current, the k_λ (0.36) one is the largest (0.78 T). The change range of k_λ (0.98) is the least, which indicates that its flux regulation performance is poor.

In addition, the change of k_λ (0.17) is the largest (0.54 T), which is 4 times that of k_λ (0.98). However, the k_λ (0.17) one is 0.37 T with only PM excitation, which is caused by the parameters such as stator tooth width and stator yoke height remaining unchanged after the stator inner diameter increases in the calculation, resulting in the saturation of the magnetic circuit such as the stator tooth, and the reduction of flux in the magnetic circuit.

The flux regulation ratio k_Φ versus different k_λ is demonstrated in Fig. 12(b). k_Φ of k_λ (0.17) is 350%, and k_Φ of k_λ (0.98) is 130%. As a result, the flux regulation ratio k_Φ is decreased with the increment of k_λ, thus the field regulation performance is worse.

The variation of no-load back-EMF with different k_λ versus excitation current is demonstrated in Fig. 13(a).

It can be seen that the back-EMF of k_λ (0.17) with PM-only excitation is the lowest (60 V), and the back-EMF of k_λ (0.98) is close to k_λ (0.57) one, which is 127 V. When the excitation current is 21 A, the back-EMF of k_λ (0.57) is the largest (187 V). The back-EMF of k_λ (0.17) is always the least under three states such as PM-only, flux-weakening, and flux-enhancing. However, its variation range of back-EMF versus excitation current is the largest (92 V), while the variation range of back-EMF with k_λ (0.98) is the least (39 V).

In addition, the total harmonic distortion (THD) of the back-EMF is studied using Fourier decomposition, the variation of THD with different k_λ versus excitation current is illustrated in Fig. 13(b). It can be found that the THD of k_λ (0.17) with PM-only excitation is the largest (14%). The THDs of k_λ (0.17), k_λ (0.24) and k_λ (0.36) descend with the increment of positive excitation current, due to the positive excitation current extends the DC component of back-EMF. Moreover, with the positive 21 A AE current, the THD of k_λ (0.24) is the lowest (3.2%).

It can be found that the MAL/SID is the key geometric parameter affecting the axial flux. The DMRHEM with a lower MAL/SID, i.e., larger $\frac{D_{ro}}{l_{Fe}}$ tends to contribute to larger $\frac{\Phi_{\text{axial}}}{\Phi_{\text{radial}}}$ than the axial flux. Therefore, the bypass effect is better and the air gap flux regulation range is larger.

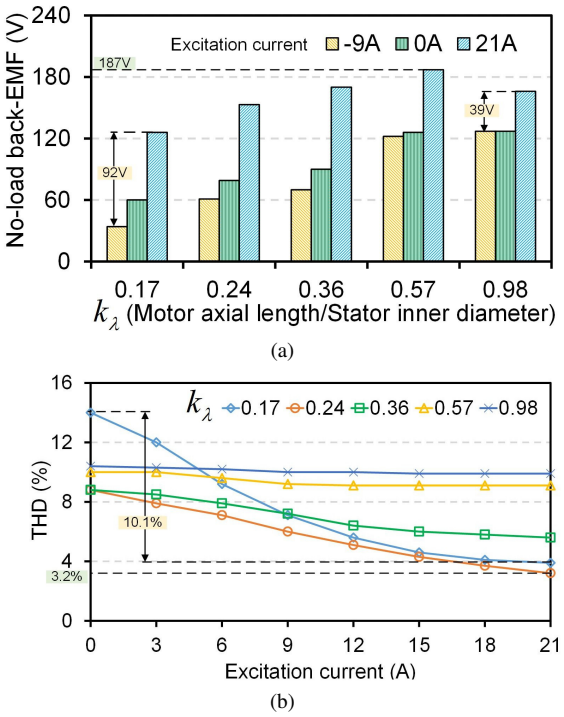

Fig. 13. Variation of (a) no-load back-EMF and (b) THD with excitation current and k_λ

5.2. Rotor pole-pair number

For spoke-type permanent magnet synchronous motors (STPMSMs), it is necessary to study the rotor pole-pair number. The STPMSM with a larger pole-pair number tends to contribute to a better flux-focusing effect. Hence, the pole-pair number also affects the bypass effect and the flux regulation performance in the DMRHEM.

In addition, when the MAL/SID and rotor outer diameter keep constant, the axial flux will be reduced with the increment of the pole-pair number and magnet thickness. With the constraint of rotor outer diameter, there is a relationship between p and magnetic thickness. In order to study the influence of variable pole-pair numbers on flux regulation performance, the constraints are stator outer diameter, stator inner diameter, and core length. Furthermore, the pole-slot combinations are flexible in the fractional-slot concentrated winding machines. It should be noted that for a DMRHEM with a higher winding factor, a larger the PM utilization ratio tends to contribute to a higher power density. According to the restriction of fractional-slot double-layer concentrated winding machines with pole-slot combinations in Table 5, with the constraint of winding factor, the machines with different pole-slot combinations are adapted. The parameters and results of machines with different pole-pair numbers are illustrated in Table 6.

Table 5. Fundamental winding factor of fractional-slot double-layer concentrated winding machine with pole-slot combinations

s/2p	**8**	**10**	**12**	**14**
6	0.866			
9	0.945	0.945	0.866	
12	0.866	0.933		0.933
15		0.866		0.951
18			0.866	0.902
21				0.866

Table 6. Parameters and results of machines with different rotor pole-pair numbers

Parameter	**8 p/9 s**	**10 p/12 s**	**14 p/15 s**	**Unit**
Rotor pole-pair number	4	5	7	
Stator slot number	9	12	15	
Stator slot body bottom width	25.8	13.8	5.3	mm
Stator slot body bottom width	33	21.6	14.2	mm
Stator yoke thickness	15.3	14.9	14.7	mm
Magnet thickness	6.25	5	3.44	mm
Winding factor	0.945	0.933	0.951	
Flux regulation ratio	271%	230%	172%	

Figure 14 shows the waveforms and spectra of no-load back-EMF for machines with different pole-slot combinations under PM only excitation. From Fig. 14(a), it can be seen that although the magnet thickness is reduced to 3.44 mm, the back-EMF of the machine with 7 pole-pair is larger than with 4 pole-pair and 5 pole-pair machines due to the better flux-focusing effect. The back-EMF of the 14 p/15 s machine is 131 V, which is 1.7 times that of 8 p/9 s (78 V). The back-EMF of the machines is sinusoidal.

In fact, under no-load conditions (with PM), there is not only the DC component in the back-EMF, but also a large number of harmonics. The main difference between the back-EMF of each machines lies in two aspects. First, the harmonics are various. According to Fig. 14(b) the harmonic orders are 3 M, 12 M, 16 M for the 14 p/15 s machine (THD is 13%). Second, the back-EMF is various. The 14 p/15 s exhibits comparatively higher back-EMF, i.e., 177 V, and the 8 p/9 s and 10 p/12 s machines, 108 V and 123 V, respectively. This is primarily attributed to the flux-focusing effect.

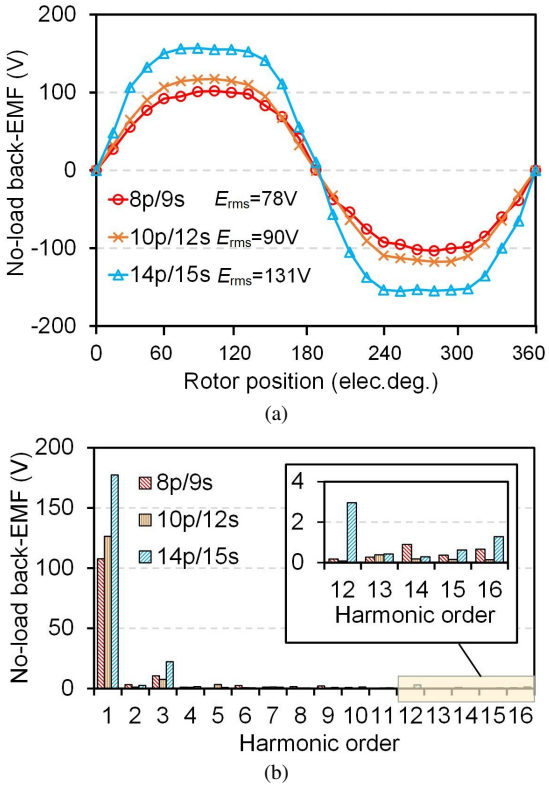

Fig. 14. No-load back-EMF with different pole-slot combinations under PM only excitation: (a) waveforms; (b) spectra

Figure 15 is presented to characterize the back-EMF with different pole-pair number versus excitation current. The field adjustment ratio is decreased with the increment of pole-pair number. For instance, the flux regulation ratio of the 4 pole-pair machine is 271%, while the flux regulation ratio of the 7 pole-pair machine is 172%. This is also consistent with the above analytical results.

Consequently, due to the increment of back-EMF, the core length can be reduced. From the MAL/SID perspective, it is beneficial to improve the bypass effect and thus extend the flux regulation range. In addition, for STPMSMs, the machine with a larger pole-pair number could improve the air gap flux, and reduce the core length, but weaken the axial bypass effect. Therefore, it could be said that these major design parameters should be carefully considered in the HEM design.

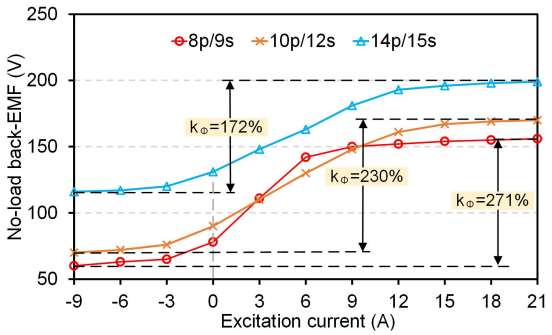

Fig. 15. The variation of back-EMF with various rotor pole-pair numbers versus AE current

6. The thermal and mechanical design

The temperature field of the motor was studied and analyzed. The boundary condition is an ambient temperature of 25°C. The convective heat transfer coefficient on the surface of the casing and end caps is 14 W/(m^{2}K). The main way to dissipate heat from the motor is through natural convection heat exchange with the outside world through the casing and end caps. Consider the influence of the contact gap between the casing and the stator core on heat dissipation. In the finite element model, the air gap between the casing and the stator core is 0.07 mm. The steady-state temperature field under the rated conditions of the motor is calculated and analyzed, and the temperature field distribution of the motor under the rated conditions is obtained, as shown in the Fig. 2 and Fig. 3.

As can be seen from Fig. 16, under the rated conditions, since the excitation winding is in full contact with the end cap, the excitation winding can fully dissipate heat. As a result, the maximum temperature of the excitation winding reaches 130°C, while the temperature of the stator winding reaches 118°C. Due to the large eddy current loss of the solid pole of the rotor and the permanent magnet, and the limited heat dissipation of the rotor, the maximum temperature of the rotor and permanent magnet reaches 157°C, see Fig. 17. The permanent magnet of the motor rotor adopts N35EH, and the maximum allowable operating temperature is about 200°C. The insulation heat resistance class of the motor is H, and the maximum allowable temperature is 180°C. To sum up, the thermal design of the motor is feasible.

The density, and Young's modulus of motor stator core material are 7 650 kg/m^3, 0 Gpa. The modal analysis of the motor is carried out by the finite element method, and the modal vibration shape and the natural frequency of the motor are obtained as shown in Fig. 18 and Table 2.

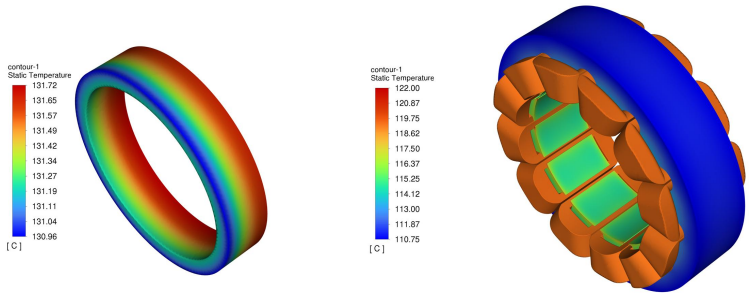

(a) (b)

Fig. 16. Temperature of excitation coils and armature coils under rated conditions

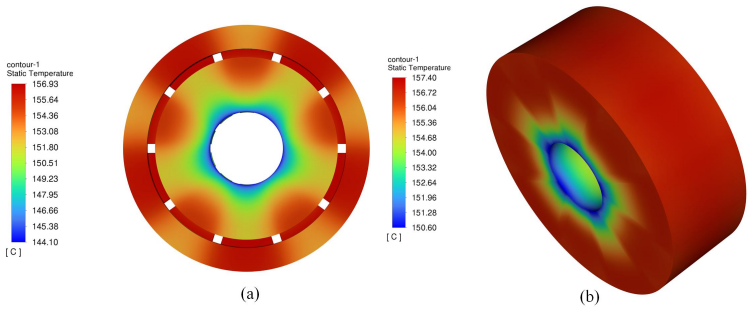

(a) (b)

Fig. 17. Temperature of disc magnetic ring and rotor under rated conditions

The higher the natural frequency, the less likely the motor will resonate. As can be seen from Table 7, the natural frequencies increase with the increasing order of vibration modal.

Table 7. The modal natural frequency of motor with different k_λ

Modal order k_λ	**2**	**3**	**4**	**5**	**6**	**Unit**
0.17	498	1343	2415	3517	4098	Hz
0.24	559	1492	2651	3798	4369	Hz
0.36	663	1749	3061	4304	4889	Hz
0.57	785	2038	3495	4796	5366	Hz
0.98	923.2	2349	3927	5233	5761	Hz

In addition, the natural frequency increases with k_λ of the motor. Therefore, increasing k_λ can greatly increase the natural frequency of the motor and reduce the influence of the natural frequency on the vibration. The basic mechanical design parameters of RAHEM are shown in Table 8.

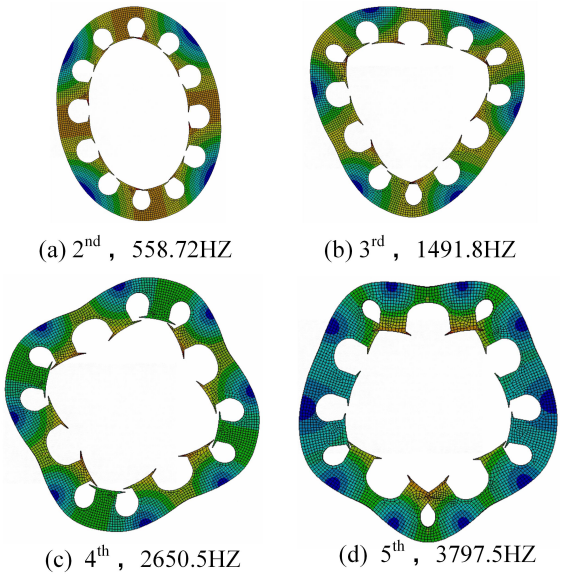

Fig. 18. The modal vibration shape and the natural frequency of motor

Table 8. Basic mechanical design parameters of RAHEM machine

Parameters	Value	Unit
Rated speed	500	r/min
Pole number	10	
Air-gap length	0.5	mm
PM volume	10 000	mm^3
PM length	40	mm
PM thickness	5	mm
Stator slot number Z	12	
Slot body height	17.6	mm
Slot body bottom width	13.8	mm
Slot wedge maximum width	21.6	mm

7. Summary of key performance of DMRHEM

The axial flux hybrid excitation motor has the advantages of low speed, high torque and short axial length. The RAHEM structure is used in low-speed electric vehicles in wheel hub motor. Combined with the driving characteristics and the performance requirements of the drive motor, the electromagnetic performance indicators of the RAHEM are shown in Table 10.

In order to analyze the main electromagnetic performance of the motor, the cogging torque, load torque and the eddy current loss are shown. The power factor is 0.95 and the efficiency is 96%. The load conditions are 500 r/min, 150 V, and 5 A axial excitation current. Figure 19 shows the cogging torque of the motor, and Fig. 20 shows the load torque.

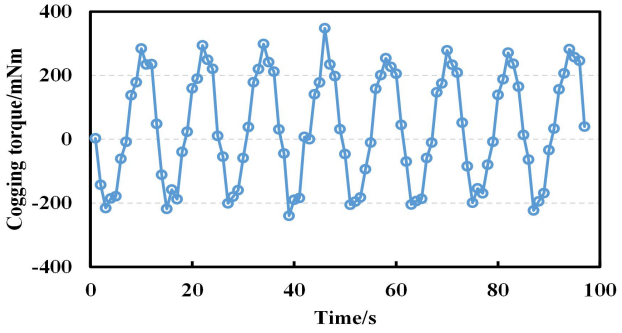

Fig. 19. Cogging torque

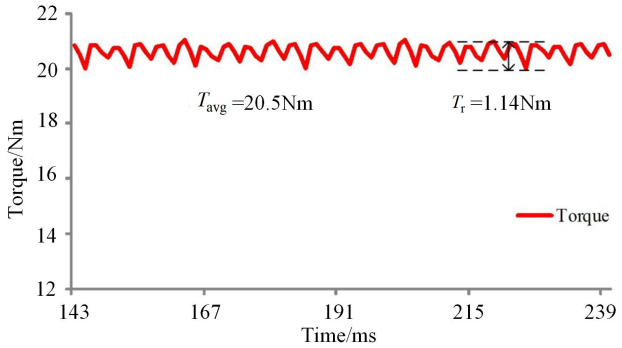

Fig. 20. Load torque

The torque is computed based on the Energy method. Compared to the traditional PMSM, the coupling mechanism between the axial flux and radial flux is more complex, and thus the torque formulation is more complex. At present, the control strategy of the motor is mostly used for the *d*–*q* coordinate. Therefore, the formulation of voltage, flux linkage, and torque is derived and shown in Table 9 and Formulas (17)–(19).

The voltage formulation of the RAHEM is:

$$\begin{cases} u_d = R_s i_d + \dfrac{\mathrm{d}y_d}{\mathrm{d}t} - \omega y_q \\ u_q = R_s i_q + \dfrac{\mathrm{d}y_q}{\mathrm{d}t} + \omega y_d \end{cases}. \tag{17}$$

The flux linkage formulation of the RAHEM is:

$$\begin{cases} y_d = L_d i_d + M_{sf} I_f + y_{pm} \\ y_q = L_q i_q \end{cases}. \tag{18}$$

The torque formulation of the RAHEM is:

$$T_{em} = \frac{3}{2} p y_{pm} i_q + \frac{3}{2} p M_{sf} I_f i_q + \frac{3}{2} p (L_d - L_q) i_d i_q. \tag{19}$$

For eddy current loss, the rotation contains the rotor, magnetic rings and PMs. The material of the rotor and magnetic rings are steel 10 with electrical conductivity and solid structure. Compared to PMs, the eddy current loss of the rotor and magnetic rings is larger, and the loss is increased with the current, as shown in Table 11.

Table 9. Dimension parameters of RAHEM

Parameter	Meaning
$u_{d/q}$	The voltage of $d/q-$axis
R_s	The synthetic magnetic resistance of d and $q-$axis
$i_{d/q}$	The current of d/q-axis
$y_{d/q}$	The flux of $d/q-$axis
$L_{d/q}$	The self-inductance of $d/q-$axis
M_{sf}	The mutual inductance between armature windings and excited windings
I_f	The excitation current
y_{pm}	The flux of permanent magnets

Table 10. Design performance indicators of RAHEM

Parameters	Value	Unit
Rated power	3.5	Kw
Rated torque	> 20	Nm
Rated speed	500	r/min
Rated voltage	150	V
Axial length of core	< 100	mm

Table 11. Eddy current loss

Axial excitation current	Rotor core and PM	Magnetic rings	Unit
0 A	113	9	w
5 A	135	13.2	w
10 A	174.5	15.4	w
15 A	208	19	w
20 A	224	22	w

8. Conclusions

To enhance the field adjustment capability of RAHEMs, a disc magnetic ring is proposed in this paper. Besides, by combining the magnetic circuit method and numerical analysis method, the influence of key parameters on field adjustment capability is determined. Finally, based on the FEM, the results are as follows:

1. The proposed DMRHEM can enhance the air-gap field adjustment range. Its field weakening capacity is 9 times better that of the RAHEM. The field adjustment ratio is 1.5 times higher than that of RAHEM. Hence, the field adjustment capability of the proposed DMRHEM is better than the RAHEM.
2. For the proposed DMRHEM, the lower the MAL/SID or the fewer the rotor pole-pair number, the larger the field adjustment range. The field adjustment range of the 0.17 MAL/SID is 4 times that of the 0.98 one. The flux regulation range of the 4 pole-pair is 1.6 times that of the 7 pole-pair counterpart. In addition, the increment of a rotor pole-pair number is beneficial to enhance the air-gap density and reduce the core length, but results in the weakening of the axial bypass effect. It can be found that there is a trade-off between enhancing the air-gap density and improving the flux regulation capability.

References

[1] Qiu H., Zhang Y., Yang C., Yi R., *Performance analysis and comparison of PMSM with concentrated winding and distributed winding*, Archives of Electrical Engineering, vol. 2, no. 69, pp. 303–317 (2020), DOI: 10.24425/aee.2020.133027.

[2] Capponi F., Borocci G., Donato G., Caricchi F., *Flux regulation strategies for hybrid excitation synchronous machines*, IEEE Trans. Ind. Appl., vol. 51, no. 5, pp. 3838–3847 (2015), DOI: 10.1109/TIA.2015.2417120.

[3] Liu X., Li Y., Liu Z., Ling T., Luo Z., *Optimized design of a high-power-density PM-assisted synchronous reluctance machine with ferrite magnets for electric vehicles*, Archives of Electrical Engineering, vol. 66, no. 2, pp. 279–292 (2017), DOI: 10.1515/aee-2017-0021.

[4] Amara Y., Vido L., Gabsi M., Hoang E., Ahmed A.H.B., Lecrivain M., *Hybrid excitation synchronous machines: Energy-efficient solution for vehicles propulsion*, IEEE Trans Veh. Technol., vol. 58, no. 5, pp. 2137–2149 (2008), DOI: 10.1109/VPPC.2006.364367.

[5] Hao H., Ziqiang Z., Wei H., *Investigation of partitioned stator hybrid excited switched flux machines with different rotor piece numbers*, Proceedings of the CSEE, vol. 41, no. 16, pp. 5715–5727 (2019).

[6] Capponi F., Borocci G., Donato G., Caricchi F., *Flux regulation strategies for hybrid excitation synchronous machines*, IEEE Trans. Ind. Appl., vol. 51, no. 5, pp. 3838–3847 (2015), DOI: 10.1109/TIA.2015.2417120.

[7] Wu Z., Fan Y., Chen H., Wang X., *Electromagnetic force and vibration study of dual-stator consequent-pole hybrid excitation machine for electric vehicles*, IEEE Trans Vehicular Technology, vol. 70, no. 5, pp. 4377–4388 (2021), DOI: 10.1109/TVT.2021.3075461.

[8] Qiu H., Yu W., Tang B., Mu Y., Li W., Yang C., *Study on the influence of different rotor structures on the axial-radial flux type synchronous machine*, IEEE Trans. Ind. Electron., vol. 65, no. 7, pp. 5406–5413 (2018), DOI: 10.1109/TIE.2017.2784339.

[9] Zhao X., Niu S., Zhang X. Fu W., *Flux-Modulated Relieving-DC-Saturation Hybrid Reluctance Machine With Synthetic Slot-PM Excitation for Electric Vehicle In-Wheel Propulsion*, IEEE Transactions on Industrial Electronics, vol. 68, no. 7, pp. 6075–6086 (2021), DOI: 10.1109/TIE.2020.2996140.

[10] Li Y., Yu Z., Meng H., Wang J., Jing Y., *Design and Optimization of Hybrid-Excited Claw-Pole Machine for Vehicle*, IEEE Transactions on Applied Superconductivity, vol. 31, no. 8, pp. 1–4 (2021), DOI: 10.1109/TASC.2021.3094433.

[11] Wang D., Wang B., Zhang F., Peng C., *Design Consideration of AC Hybrid-Excitation Permanent-Magnet Machine with Axial Stator Using Simplified Reluctance Network*, IEEE Transactions on Industrial Electronics, vol. 69, no. 12, pp. 12447–12457 (2022), DOI: 10.1109/TIE.2021.3135614.

[12] Wang X., Fan Y., Chen Q., Wu Z., *Magnetic Circuit Feature Investigation of a Radial–Axial Brushless Hybrid Excitation Machine for Electric Vehicles*, IEEE Transactions on Transportation Electrification, vol. 9, no. 1, pp. 382–393 (2023), DOI: 10.1109/TTE.2022.3199435.

[13] Zhang Z., Yan Y., Yang S., Bo Z., *Principle of operation and feature investigation of a new topology of hybrid excitation synchronous machine*, IEEE Transactions on Magnetics, vol. 44, no. 9, pp. 2174–2180 (2008), DOI: 10.1109/TMAG.2008.2000513.

[14] Amara Y., Vido L., Gabsi M., Hoang E., Ben Ahmed A.H., Lecrivain M., *Hybrid excitation synchronous machines: energy-efficient solution for vehicles propulsion*, IEEE Transactions on Vehicular Technology, vol. 58, no. 5, pp. 2137–2149 (2009), DOI: 10.1109/TVT.2008.2009306.

[15] Hongbo Qiu, Yuqing Zhang, Xiaolu Ma, Cunxiang Yang, *Operating principle and performance analysis of a novel flux–torque regulation hybrid excitation machine with axial–radial magnetic circuit using magnetic network*, IET Electric Power Applications, vol. 17, no. 6, pp. 824–834 (2023), DOI: 10.1049/elp2.12306.